ADVANCED SUSTAINABLE SYSTEMS
www.advsustainsys.com

Apple Tree Root-Derived Biochar/Iron Oxide Triphasic Nanocomposite for Wastewater Treatment and Microwave Absorption

Mahsa Mahmoodi, Bagher Aslibeiki, Sagnik Ghosh, Leila Hasani, Sawssen Slimani, Luca Vattuone, Davide Peddis,* and Tapati Sarkar**

In this work, two major sources of pollution: (1) Water pollution due to heavy metals, and (2) Electromagnetic wave (EMW) pollution, often regarded as the fourth category of pollution (after air, water, and soil pollution) are addressed. A unique bio-based triphasic nanocomposite (Fe_3O_4/α-Fe_2O_3/carbon) is synthesized and its superior properties are demonstrated to address both types of environmental pollution. The nanocomposite, derived from lightweight apple tree roots, is used for Pb (II) ion removal from aqueous solutions via adsorption and magnetic separation. The biomass-derived highly porous biochar decorated with iron-oxide showed adsorption efficiency of nearly 100% and corresponding capacity of 149 $mg.g^{-1}$ under optimal conditions for initial Pb (II) concentration of 50 $mg.L^{-1}$. Furthermore, a remarkable adsorption capacity of 731 $mg.g^{-1}$ is achieved using lower amount of the adsorbent for a slightly lower efficiency (97%). In addition, the mesoporous composite showed excellent EMW absorption efficiency with effective absorption bandwidth of 7.8 GHz and reflection loss of −61.7 dB, arising from very good impedance matching, and high dielectric and magnetic losses. This work establishes the multifunctional properties of the synthesized composite, and addresses the UN Sustainable Development Goal (SDG) 6 (Clean water and sanitation) and SDG 13 (Climate action, including pollution management).

1. Introduction

In 2015, the United Nations ratified 17 Sustainable Development Goals (SDGs) with the aim to build a sustainable development strategy by 2030.[1] These 17 goals target different aspects of human existence. In practice, however, it is unlikely that we will reach the targets by 2030 unless the current pace of research is accelerated many folds. For this, developing multifunctional materials that can be used to tackle more than one SDG appears to be a promising approach. In particular, this study focuses on the synthesis of a new triphasic nanocomposite that shows promising properties to tackle two SDGs: SDG 6 and SDG 13. These two SDGs, SDG 6 (availability of clean water and sanitation for all) and SDG 13 (climate action and pollution control), are inter-related and demand our immediate attention as the world grapples with increasing water and climate crisis.[2,3]

M. Mahmoodi, B. Aslibeiki
Faculty of Physics
University of Tabriz
Tabriz 5166616471, Iran
E-mail: b.aslibeiki@tabrizu.ac.ir

B. Aslibeiki, S. Ghosh, T. Sarkar
Department of Materials Science and Engineering
Uppsala University
Uppsala Box 35, SE-75103, Sweden
E-mail: tapati.sarkar@angstrom.uu.se

L. Hasani
Department of Landscape Engineering
Faculty of Agriculture
University of Tabriz
Tabriz 5166616471, Iran

S. Slimani, D. Peddis
Department of Chemistry and Industrial Chemistry & Genova
INSTM RU, nM2-Lab
University of Genova
Genova 16146, Italy
E-mail: Davide.Peddis@unige.it

S. Slimani, D. Peddis
Institute of Structure of Matter
National Research Council, nM2-Lab
Via Salaria km 29.300, Monterotondo Scalo, Roma 00015, Italy

L. Vattuone
Dipartimento di Fisica
Università degli Studi di Genova
Via Dodecaneso 33, Genova I-16146, Italy

L. Vattuone
IMEM-CNR
UOS di Genova
Via Dodecaneso 33, Genova 16146, Italy

The ORCID identification number(s) for the author(s) of this article can be found under https://doi.org/10.1002/adsu.202400549

DOI: 10.1002/adsu.202400549

The original categories of pollution constitute air, water, and soil pollution. In addition, with the recent rise in wireless telecommunication devices, electromagnetic interference (EMI) has come up as the fourth category of pollution.[4]

Water crisis constitutes the health of the aquatic ecosystem, and is directly related to the health of all life forms on Earth. This includes underground and surface water resources, and affects all kinds of animal and plant habitats. Protecting water resources is, therefore, critical for sustainability and continuation of life as we know it. However, in many developing countries that suffer from water shortages, polluted water from sewage systems enters natural reservoirs directly without proper control, thereby making plant, animal, and human habitats unsustainable. Primary among water pollutants are heavy metal ions whose presence in drinking water has harmful effects on human health[5] such as reduced growth of organs, cancer, and disorder in the body's nervous and defense systems. In particular, lead, a very common toxic heavy metal, can cause retardation and learning disorders, memory disorders, damage to the nervous system, and movement disorders such as seizures or hyperactivity in infants and young children. In more severe cases, heavy metal ions cause irreparable brain damage.[6,7] Children are more exposed to the risks of heavy metals in water and food than adults because they consume more water and food than their body weight. Therefore, to reuse industrial water and prevent environmental risks, affordable methods for wastewater recovery and treatment are crucial.

Heavy metals can be removed from water by a wide variety of methods such as distillation, coagulation, membrane processes, ion exchange, reverse osmosis, biological treatment, chemical oxidation, solvent extraction, and electrochemical techniques.[8,9] Some of these methods are not cost-effective, and others can harm the environment due to the production of toxic by-products.[10] On the other hand, iron oxides like magnetite (Fe_3O_4), hematite (α-Fe_2O_3), and maghemite (γ-Fe_2O_3) exist in nature and have been widely used to remove heavy metals from wastewater. Hematite nanoparticles are one of the most stable natural compounds in the Earth's crust and they have been widely studied as an adsorbent.[11] It has favorable qualities such as its ability to harvest light, stability in aquatic environments, abundance in nature, and safe environmental properties.[12] However, hematite has some inherent shortcomings also, such as poor surface oxygen evolution reaction kinetics, and is only weakly magnetic, which seriously limits its adsorption capability and ability to promote magnetic separation.[13] Magnetic nano-adsorbents have the advantage of allowing magnetic separation of solids from liquids due to their response to external magnetic fields.[14] Fe-based nano-adsorbents have also shown high adsorption efficiency due to their high surface-to-volume ratio, while also being easy to synthesize, compatible with the environment, and relatively cheap.[15] Their performance as heavy metal adsorbents is further increased by synthesizing composites of activated carbon/magnetic materials compared to single phase magnetic nanoparticles (MNPs). To synthesize such composite systems, bioactive carbon is pyrolyzed under oxygen-free conditions, and has attracted much attention due to the advantages of high porosity, wide availability, and being economically favorable. Till date, several biomasses like sawdust,[16] sunflower waste carbon,[17] coffee grounds,[18] orange peel,[19] citrus lemon wood,[20] papaya peel waste,[21] corncob,[22] and vine shoots,[23] have been effectively used. Compared to these, wood is one of the most basic sources of activated carbon. To rejuvenate agricultural lands and gardens, old trees are uprooted every year. The abundant presence of mesopores in tree roots increases its potential for producing activated carbon with high surface area.

With regard to the fourth category of pollution, wireless communication devices operating in the microwave frequency region emit harmful electromagnetic (EM) radiation. EMI occurs when stray EM radiation interferes with other devices resulting in data corruption, performance loss, and critical device failure. EMI pollution has far-reaching consequences including threat to aviation security,[24] deactivation of vital life support systems like implantable cardioverter defibrillator,[25] and damage to computerized transport supervision systems.[26] Furthermore, studies conducted by the United States of America National Toxicology Program has painted a grim picture of EMI pollution by classifying electromagnetic waves (EMWs) as possible human carcinogens.[27,28] 5G waves are absorbed easily by trees, humans, and animals. Once absorbed, the EMW can interfere with brain activity, cell division, and heartbeat regulation since these biological activities are all controlled by electrical impulses.[29] To counter the menace of EMI, EMW absorbing materials are in high demand. Materials with wide absorption bandwidth, low thickness, light weight, and high absorption efficiency are preferred as microwave absorbers.[30] The absorption efficiency of an EMW absorber is measured by its reflection loss (RL in dB). RL values less than -10 dB are required for effective EMW absorption. In literature, ferrites and ferrite-based composites have been used extensively as microwave absorbers. Ni et al.[31] synthesized Fe_3O_4 nanocrystals and paraffin wax composites. The composite with 30% volume fraction of Fe_3O_4 exhibited the best reflection loss of −21.2 dB at 8.16 GHz. Ji et al.[32] fabricated Fe_3O_4/α-Fe_2O_3 composite and found a maximum reflection loss value of −43.1 dB at a thickness of 2.0 mm with an effective absorption bandwidth of 3.4 GHz. Other than the standard ferrites, carbon-based materials are also attractive as microwave absorbers due to their low weight, high porosity, adjustable frequency range, and large surface area with surface polar groups. The presence of these polar groups at the surface results in polarization mechanisms that attenuate the incoming EM radiation.[33] Activated carbon fibers and Fe_3O_4 composite has been found to exhibit a maximum RL value of −44.3 dB at 10 GHz with effective absorption bandwidths of 4.8 and 1.1 GHz. However, to the best of our knowledge, EMW absorbing properties of a triphasic composite consisting of Fe_3O_4/α-Fe_2O_3/activated carbon have not been studied before.

Activated carbon obtained from the roots of apple trees shows textural features consisting of a large number of mesopores and micropores. Physical and chemical activation processes can also be used to create numerous porous structures in these materials that can trap heavy metals.[34,35] At the same time, these pores contribute to multiple reflections and refractions of microwaves, resulting in the attenuation of microwave energy. Therefore, porous carbon materials obtained from natural biomass have the potential to be used as absorbing materials for both heavy metals and microwaves. In addition, making composites with nanostructured iron oxides results in enhanced functionalities. Iron oxide nanoparticles have a large surface area and depending on the synthesis methods, a proper mesostructure (i.e., presence

of pores and voids) can be obtained, making these materials of potential interest as adsorbents.[36,37] In addition, iron oxide nanoparticles (i.e., maghemite, magnetite, hematite), are common components in soil, sediments, water, iron, and steel industries, and are relatively easy to synthesize. In most previous studies, the separation of the adsorbent post-adsorption has been done by filtration and centrifugation methods, resulting in increased operational costs.[38,39] Furthermore, these techniques may not be able to completely separate the adsorbent from the sample thereby leading to secondary contamination. To overcome these challenges, magnetic iron oxide/activated carbon nanocomposites can be used for quick and easy separation of the adsorbents by an external magnetic field. Furthermore, according to the mechanism of EMW losses, EMW absorbing materials mainly include dielectric loss absorbing materials and magnetic loss absorbing materials. Accordingly, dielectric loss-absorbing materials combined with magnetic loss media can be a good way to develop excellent EMW-absorbing materials. The synergistic effect between the two mechanisms can help to achieve good electromagnetic absorption performances.

In this complex and fascinating scenario, this work focuses on the synthesis of Fe_3O_4/α-Fe_2O_3/activated carbon (F/α/C) triphasic nanocomposite with optimized surface, textural and magnetic features for Pb (II) ions removal from aqueous solutions. The material was synthesized using low-cost and easily available resources, making it more attractive and increasing its potential for use in applications. The morphology, structure, and magnetic properties of the composite were analyzed by Fourier transform infrared spectroscopy (FTIR), adsorption and desorption analysis (Brunauer-Emmett-Teller (BET) method), vibrating sample magnetometry (VSM), X-ray photoelectron spectroscopy (XPS), X-ray diffraction (XRD), Raman spectroscopy, field emission scanning electron microscopy (FESEM), and energy dispersive X-ray spectroscopy (EDS). The effectiveness of the composite as an adsorbent for Pb (II) was studied by exploring in detail the effect of pH, reaction time, adsorbent dose, initial concentration of toxic ions, and bath temperature. The adsorption kinetics was investigated, linear and non-linear models were applied to the data, and the adsorption thermodynamics and reusability were explored. Finally, the potential of the same composite as a microwave absorber was investigated by characterizing its microwave absorption properties using a vector network analyzer.

2. Results and Discussion

2.1. Fe_3O_4/α-Fe_2O_3/Activated Carbon (F/α/C) Triphasic Nanocomposite: Structure and Morphology

The FTIR data for activated carbon obtained from apple tree roots, and F/α/C magnetic nanocomposite are shown in inset (a) of Figure S1 (Supporting Information). Both spectra show a broad peak corresponding to O-H stretching at ≈3426 cm^{-1},[40] due to the presence of hydroxyl groups on the surface of materials. The absorption peaks at 1699 cm^{-1} and 1564 cm^{-1} are attributed to the stretching vibrations of C=C groups of unsaturated aliphatic and carbonyl/carboxyl structures, respectively. The peaks at 1197 cm^{-1} and 898 cm^{-1}, also present in both spectra, can be assigned to the vibrations of C-O-C and C-H functional groups, respectively. All these peaks can be ascribed to the activated carbon. The spectrum of the nanocomposite shows two absorption peaks at 565 cm^{-1} and 447 cm^{-1} due to the Fe-O bonds in magnetite/maghemite and hematite, respectively. These observations prove the presence of magnetic spinel iron oxide on the activated carbon (in agreement with the FESEM results, Figure S2, Supporting Information). Thus, the FTIR spectra indicate that the F/α/C powders have functional groups of O-H, C-O, and Fe-O, which can effectively cause heavy metals ions adsorption through formation of chemical bonds.[41,42]

Figure S2a (Supporting Information) shows the morphology of the apple tree roots derived activated carbon confirming the highly porous structure of the activated carbon. The rough surface contains holes of different shapes and sizes that, combined with MNPs, can trap heavy metal ions.[43] Spinel iron oxide nanoparticles are anchored on the activated carbon as single spheres and agglomerates (Figure S3, Supporting Information). The results of EDS analysis (Figure S2c-g, Supporting Information) confirm the presence of iron, carbon, and oxygen in the composite, and the distribution of MNPs on the carbon surface.

The specific surface area directly affects the adsorption capacity of a material; therefore, nitrogen adsorption-desorption process was used to determine the specific surface area of the F/α/C nanocomposite surface. Nitrogen gas adsorption and desorption and Barrett-Joyner-Halenda pore-size distribution curves are shown in Figure S4a,b (Supporting Information). The obtained high specific surface area of ≈649 $m^2\ g^{-1}$, with an average mesopore diameter of ≈2.2 nm suggests the suitability of the composite as an adsorbent. It is worth to underline that these results confirm that the use of an activator during calcination induces a highly mesoporous structure with increased specific surface area.[44]

To better understand surface interactions and material behavior in various environments, the point of zero charge (pH_{pzc}) is measured. The pH_{pzc} represents the pH at which the surface of a nanocomposite has no net electrical charge, meaning the density of positive charges is equal to the density of negative charges. This measurement allows us to see how the material will interact with its surroundings. Figure S4c,d (Supporting Information) show the point of zero charge (pH_{pzc}), which is 5.60 and 7.25 for activated carbon and the F/α/C nanocomposite, respectively. These results indicate that by anchoring MNPs on the surface of the carbon, the efficient pH region for adsorption shifted to higher pH values. In fact, at low pH, the surface of the iron oxide particles is positively charged due to protonation of hydroxyl groups, which leads to a reduced adsorption efficiency due to repulsion between the positively charged surface and the heavy metal cations. However, at pH ≥ 7, the F/α/C surface becomes negatively charged, enhancing adsorption efficiency through electrostatic attraction with the positively charged heavy metal cations. On the other hand, one can expect that a reduction in pH_{pzc} after adsorption suggests that the adsorbent's surface, initially containing a significant amount of hydroxyl groups, has undergone changes due to interactions with heavy metal ions. This change typically reflects a strong interaction between the adsorbent and the adsorbate, often leading to efficient adsorption. The presence and activity of surface hydroxyl groups are critical as they directly influence the surface charge and, consequently, the adsorption behavior.[45] To understand better the effect of pH on the adsorption mechanism, bath

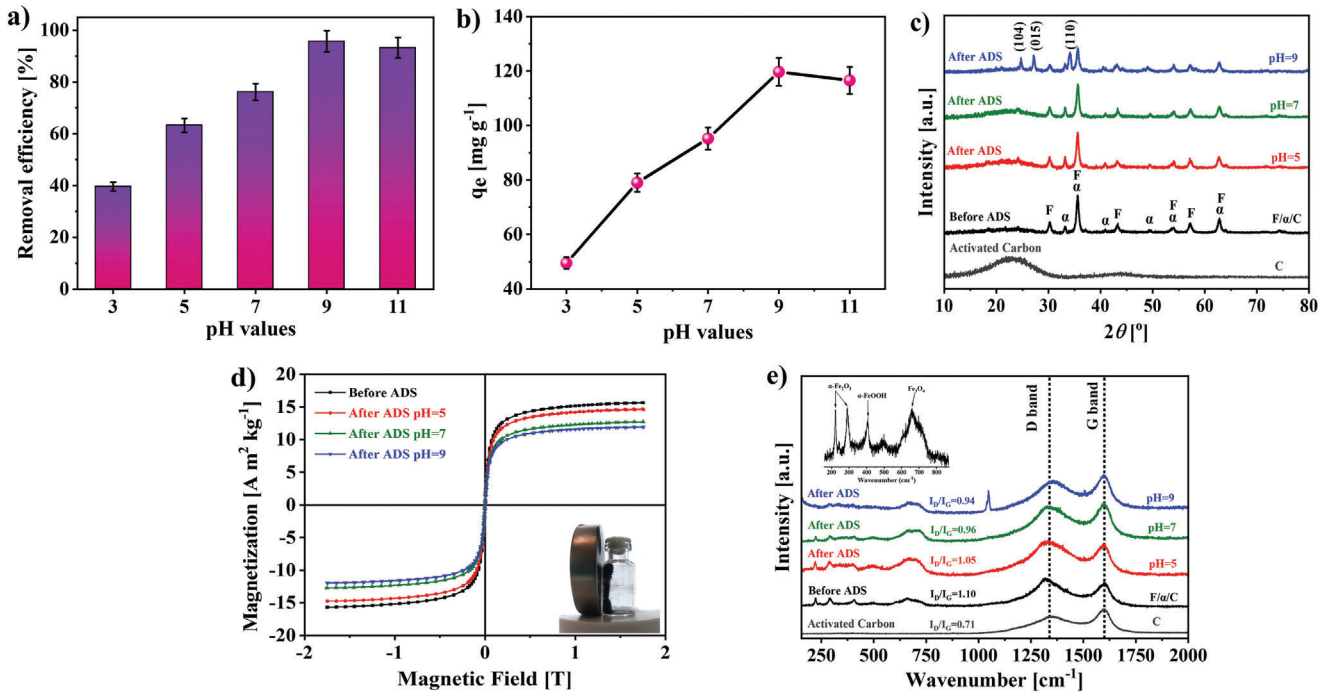

Figure 1. Effect of pH on a) removal efficiency and b) adsorption capacity. c) XRD patterns showing peaks corresponding to Fe_3O_4 and α-Fe_2O_3 marked as "F" and "α", respectively, d) Magnetic hysteresis loops, inset shows easy removal of the composite by a permanent magnet from water, and e) Raman spectra of pure activated carbon and F/α/C nanocomposite before and after adsorption of Pb (II) at different pH values. Inset in (e) shows the spectra for the composite before adsorption, in the wavenumber range of 150 cm^{-1} to 850 cm^{-1}.

experiments were performed under different pH values, followed by detailed structural and magnetic characterization after adsorption at pH values of 5, 7, and 9.

2.2. Adsorption Studies

Adsorption experiments were performed using bath experiments by varying different parameters like pH of solution, contact time, concentration of toxic element, adsorbent dosage, temperature, and reusability of the adsorbent to find the ultimate optimal conditions for Pb (II) removal.

2.2.1. Impact of pH

Figure 1a,b show the pH-dependent removal efficiency and adsorption capacity of the F/α/C nanocomposite. Under acidic pH values, the metal ions are more stable and it is difficult to remove them from aqueous solution. In contrast, basic pH values lead to a decrease in the stability of the metal ions and increase their removal efficiency from water.[46] The presence of a negatively charged surface of the composite reduces the electrostatic repulsion between the adsorbent and Pb (II) ions, increasing the metal removal efficiency and adsorption capacity.[47] Figure 1a shows the gradual increase of Pb (II) removal efficiency from ≈39% to ≈96% when the pH was increased from 3 to 9. The active binding sites on the adsorbent surface are protonated at low pH, and as a result, the binding of metal ions is reduced due to electrostatic repulsion. The increase in pH and the activation of functional groups on the surface of the adsorbent lead to an increase in the adsorption of Pb (II) ions. At pH = 9, the surface of the adsorbent becomes negatively charged due to the presence of the OH-and COO- functional groups, and the exchange of ions between the functional groups and metal cations takes place. At pH = 9, precipitation of metal ions occurs in the form of hydroxides (Pb^{2+} + $OH^- \rightarrow Pb(OH)_2$) affecting the adsorption capacity, due to decrease of Pb (II) concentration in solution. The forces of attraction tend to increase the binding of lead to the nanocomposite during precipitation. Other studies have also reported similar findings.[48–50] The maximum efficiency and adsorption capacity were obtained at pH = 9, where the removal efficiency and q values are 96% and 120 mg g^{-1}, respectively.

To study the adsorption mechanism under acidic and basic environments, XRD of the powders were analyzed before and after adsorption for selected pH values of 5, 7, and 9, as shown in Figure 1c. Reflections corresponding to the Fe_3O_4 phase with an inverse spinel structure were observed (standard card 96-900-2319), together with α-Fe_2O_3 phase (standard card 96-900-9783). At pH = 9, the XRD pattern shows the formation of hydrocerussite, $Pb_3(CO_3)_2(OH)_2$ which was denoted by the Bragg peaks (110), (104), and (015).[51,52] However, at pH = 5 and 7, there is no trace of this insoluble precipitate, which suggests that under basic conditions, the main adsorption mechanism could be precipitation. Furthermore, the obtained pH_{pzc} value for the composite (≈7.25) suggests dominance of positive charges at pH values less than this point and leakage of hydroxyl groups, which are responsible for the formation of white lead.

As seen in Figure 1d, the magnetic hysteresis loops show superparamagnetic behavior (i.e., zero remanence and zero

coercive field), both before and after adsorption at selected pH values of 5, 7, and 9. The pH value, however, has some effect on the saturation magnetization (M_S), which decreases with increasing pH. The saturation magnetization of the composite before adsorption experiments was 16 $Am^2\ kg^{-1}$, and it reduced to 15, 13, and 12 $Am^2\ kg^{-1}$ after adsorption at pH = 5, 7, and 9, respectively. It is worth noting that the presence of diamagnetic carbon is the main reason for the observed reduced magnetization of the composite before adsorption, compared to bulk Fe_3O_4 (93 $Am^2\ kg^{-1}$).[53] However, this is not critical for our purpose because magnetic separation experiments showed rapid removal of the adsorbent from solution even after several adsorption cycles. The strength of the N42 Neodymium (NdFeB) permanent magnet that was used to separate the nanocomposite is ≈0.23 T. Interestingly, it could be possible to reduce the strength of the permanent magnet used for the separation process by using ring magnets instead of block magnets.[54] The reduction of saturation magnetization at pH = 5 and 7 can be ascribed to the adsorption of Pb (II) ions and possible water molecule trapping, while at pH = 9, precipitation of lead carbonate could be the other reason for further magnetization reduction. We recognize that the observed behavior is quite peculiar and further investigations are in progress to clarify this.

To provide qualitative information about the presence and stability of the characteristic functional groups, the Raman spectra of the activated carbon and the nanocomposite before and after adsorption at selected pH values were performed and are shown in Figure 1e. Two distinct peaks in the spectrum of activated carbon centered at 1592 cm^{-1} (G-band) and 1350 cm^{-1} (D-band) are characteristic of graphite and indicate lattice defects, respectively. The degree of graphitization was assessed using the I_D/I_G peak intensity ratio.[55] The evaluated values for the original activated carbon and the magnetic nanocomposite were 0.71 and 1.1, respectively. This indicates that the degree of graphitization of activated carbon can be modified with MNPs decoration, however, this effect still needs further investigation. As seen in the inset in Figure 1e, few intense peaks are observed for the composite before adsorption in the range of 150 cm^{-1} to 850 cm^{-1}, which are related to the magnetic component of the adsorbent.[56] The peaks centered at 222 cm^{-1} and 289 cm^{-1} correspond to α-Fe_2O_3, the peak at 405 cm^{-1} corresponds to FeO(OH), and the observed peaks at 494 cm^{-1} and 658 cm^{-1} indicate Fe_3O_4, which are in agreement with the XRD results. When the pH value reaches a specific range corresponding to alkaline solutions, the hydroxyl and carboxyl functional groups are hydrolyzed and affect the surface charge of activated carbon. The peaks at 146 cm^{-1} and 1044 cm^{-1} for pH = 9 indicate formation of $Pb_3(CO_3)_2(OH)_2$ in agreement with the XRD pattern.[57,58] The intensity of the peaks related to the magnetic phase decreases with increasing pH.[59,60] This is most likely due to precipitation of Pb (II) compound on the surface of the composite, which reduces the intensity of the peaks related to iron oxides. This conclusion is also supported by the decrease of Fe lines in the XPS spectrum (see Figure S7, Supporting Information).

EDS results and mapping data of the nanocomposite after adsorption at pH = 5, 7, and 9 are shown in Figure S5a-f (Supporting Information). The presence of Pb in the EDS data confirms the successful adsorption on the active sites of the adsorbent (most prominently for pH = 9). Pb (II) peak was observed at the energy of ≈2.5 keV, and its atomic percentage increased from 0.2% at pH = 5 to 1.4% at pH = 9. Figure S6 (Supporting Information) shows detailed pH dependent EDS data, which confirms the XRD, Raman, and magnetometry results. Based on the obtained results, we continued the bath experiments at pH = 9.

XPS spectra were collected for the sample before exposure to Pb, and for samples following exposure to Pb at different pH values (5, 7, and 9), and for the latter, for two different Pb concentrations (50 ppm and 210 ppm). The energy scale was calibrated using the C 1s line and setting its value to 284.5 eV (corresponding to sp2 carbon).

Inspection of the overview (Figure S7, Supporting Information) shows that Fe related lines (2p doublet as well as 3p doublet) are significantly attenuated for pH = 9 (blue and pink lines) while they are less affected for pH = 5 and pH = 7, confirming that the Pb coverage on the nanoparticles is larger for pH = 9. Further insight can be obtained by inspection of the high-resolution spectra for Pb 4f, O 1s, and C 1s lines (Figure S8, Supporting Information). The spectra are normalized on the low binding energy (BE) side.

For the bare nanoparticles not exposed to Pb, the O 1s feature has a main contribution at 530.2 eV and a shoulder at 531.5 eV. The former peak is associated to iron oxide while the one at higher BE is most likely due to OH.[61]

After exposure to Pb, a feature around 138.9 eV appears due to Pb 4f 7/2 (together with its companion at higher BE due to Pb 4f 5/2). This BE for Pb 4f is incompatible both with metallic Pb (expected at 136.7 eV) and lead oxides, PbO_2 (expected at 137 eV) and PbO (expected at 138 eV), see Table S1 (Supporting Information). Considering the uncertainty of the BE calibration, the observed BE would be compatible both with cerussite (139 eV) and hydrocerussite (138.4 eV). XRD diffraction data allows, however, to exclude the presence of hydrocerussite for pH=5 and pH=7 and therefore, we tentatively assign the species with Pb 4f at 138.9 eV to cerussite. Since the O 1s lineshape is less affected by Pb load for pH = 5 and pH = 7, this assignment is consistent with a relatively low concentration of Pb.

When the pH is increased to 9, the Pb 4f peak becomes broader and its maximum shifts to lower BE. It is thus possible to fit it adding a second contribution with a BE of 138.5 eV (green peak in the fit) which shows up for a Pb concentration of 50 ppm and becomes dominant at 210 ppm. The peak at 531.5 eV in the O 1s spectrum increases and its intensity becomes comparable with one of the main peaks at 530.2 eV. We underline that the reduction of the normalized intensity at 530.2 eV is not due to removal of iron oxides but is due to the screening by Pb deposited on the nanoparticle surface (as evident from Figure S7, Supporting Information). The feature at 531.5 eV does not decrease when pH increases, and it is thus associated with the formation of CO_3.

For the C 1s line, the decrease of the feature at 284.5 eV (due to carbon at the surface) when the pH is increased from 7 to 9 is also due to the screening by Pb at the surface of the nanoparticles. The intensity at 289.5 eV, similar to the feature at 531.5 eV, does not decrease and is thus also indicative of the formation of CO_3. The shift from 289.5 eV for 50 ppm to 289 eV for 210 ppm can be related to the increase in the fraction of hydrocerussite with respect to cerussite and is consistent with the fact that the C 1s line in CO_3^{2-} of hydrocerussite is expected at 288.9 eV and the one of cerussite at 289.5 eV.

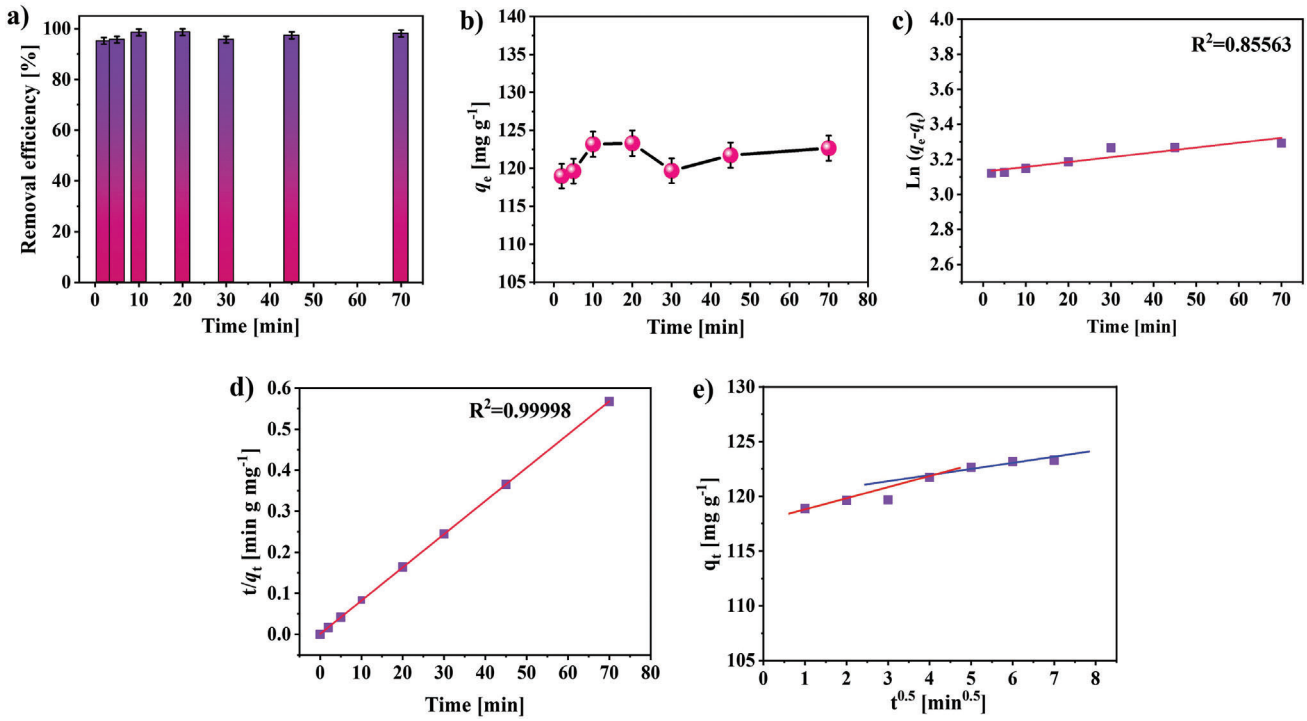

Figure 2. Effect of agitation time on a) removal efficiency, and b) adsorption capacity of Pb (II) ions by F/α/C nanocomposite. Fits of the adsorption data using c) pseudo-first-order, d) pseudo-second-order, and e) intraparticle diffusion models.

Inspection of the normalized Fe 2p lines (Figure S9, Supporting Information) indicates that the lineshapes after exposure to Pb are superimposed with the lineshape before exposure. This indicates that no significant charge transfer occurs between iron oxide nanoparticles and Pb even when the adsorbed amount has reached its maximum.

At pH = 5, by comparing the total intensity of Pb 4f with the total intensity of Fe 2p and correcting for the relative sensitivity, it is possible to estimate that the number of Pb atoms is of the order of 5% of the amount of (surface) Fe atoms. The quantification of the amount of Pb present at pH = 9 is not straightforward since the signal due to Fe is significantly attenuated when Pb load becomes significant. Using the universal mean free path for electron as a function of energy, it is possible to estimate a thickness of the order of 2 nm of Pb for pH = 9 (50 ppm) and close to 3 nm for pH = 9 (210 ppm). These values can be considered upper limits for the thickness; they are reasonable since the Fe 2p line is severely attenuated and at the kinetic energy of the corresponding photoemitted electrons (≈770 eV) their mean free path is of the order of 1.5 nm. A lower limit to the Pb amount on the surface of the nanoparticles can be crudely estimated by comparing the Pb 4f intensity at pH = 9 for 210 ppm with the one for pH = 5; the amount of Pb for pH = 9 must be at least 7 times larger than for pH = 5. This result is in good agreement with EDS data shown in Figure S5b,f (Supporting Information).

2.2.2. Impact of Contact Time and Kinetic Studies

The effect of contact time on the adsorption process was investigated in the range of 3 to 70 min under the optimal pH value of 9 (**Figure 2**a,b). The results reveal that for a contact time of only 3 min, a high removal efficiency of 95% is achieved with a corresponding q = 119 mg g^{-1}, which can be due to the presence of the functional groups and a high number of active sites in the porous structure. The adsorption efficiency and capacity in the first 20 min reaches 99% and 123 mg g^{-1}. The adsorption capacity slightly decreases with further increase in time, which can be attributed to the accumulation of ions on the surface of the adsorbent, resistance to the penetration of Pb (II) ions to the active sites of the composite, or the release of metal ions from the surface.[62,63] Therefore, 20 min was selected as the optimal time for subsequent experiments.

Investigating the adsorption kinetics can be very useful to understand the adsorption mechanism. **Table 1** shows the values of q_e, k, and correlation coefficients R^2 obtained by the fitting with pseudo-first-order (PFO), pseudo-second-order (PSO),[64] and intraparticle diffusion models kinetic models[65] (details provided in the Supporting Information).

The obtained R^2 values (fits shown in Figure 2c,d) suggest that the accuracy of the PSO model is higher than the other models. Moreover, the adsorption capacity obtained from the PSO model (123 mg g^{-1}) matches extremely well with the experimental value (123 mg g^{-1}). Typically, The PFO model assumes that physical adsorption is rate-limiting by particle adsorption, while the PSO model considers chemical adsorption as the rate-limiting mechanism of the process, describing the behavior over the entire adsorption range. In the samples under investigation, PSO kinetics indicate that the rate of ions adsorption depends on functional groups or surface binding sites. In other words, the amount of adsorption depends on the adsorption capacity, and not on the

Table 1. Obtained parameters and correlation coefficients using different linear fitting isotherm models for adsorption of Pb (II) by F/α/C nanocomposite.

Linear Isotherm Model	Parameters	R^2
Pseudo-first-order model	q_e [mg g^{-1}] = 22.868 (5)[a)]	0.85563
	k_1 [L mg^{-1}] = −0.00005 (2)	
Pseudo-second-order model	q_t [mg g^{-1}] = 121.291	0.99998
	K_2 [L mg^{-1}] = 0.00005 (4)	
	q_e [mg g^{-1}] = 123.4568 (1)	
Intraparticle diffusion	K_{d1} = 0.750	0.9998
	C_1 = 118.13	0.8976
	K_{d2} = 0.5 (1)	
	C_2 = 119.8 (7)	
Langmuir isotherm	b [L mg^{-1}] = 6.507 (1)	0.93803
	q_m [mg g^{-1}] = 109.77 (2)	
	R_L = 0.003 (1)	
Freundlich isotherm	N = 2.01 (7)	0.92228
	K_f [L mg^{-1}] = 125.80 (6)	
Temkin isotherm	B [J mol^{-1}] = 129 (5)	0.83447
	K_T [L mg^{-1}] = 2.5 (3)	

[a)] Uncertainties in the last digit are given in parentheses.

concentration of adsorbents. The better agreement with the PSO model is consistent with the absence of metallic Pb in XPS, which should be present in case of physisorption. The intraparticle diffusion model was presented by Weber and Morris,[65] where the diffusion rate is a function of the square root of time. This model (fit shown in Figure 2e) is based on the internal and external diffusion mechanisms that occur by surface adsorption. Figure 2e shows two straight lines that do not intersect the origin. The first linear fit in red corresponds to intraparticle diffusion, while the second linear fit in blue corresponds to the temporal region when stability and equilibrium has been reached.[66] The fittings indicate that the adsorption process proceeds in two separate stages. Furthermore, the fact that the plot of q_t versus $t^{0.5}$ does not cross the origin in any of the regions suggests that intraparticle diffusion is more than just a rate-controlling step and that the boundary diffusion layer actually influences the removal process. A crossover region is seen (near t = 16 min), beyond which the slope decreases and the system approaches equilibrium. This is reasonable considering that this is a dynamic process.

If the line passes through the origin, then intraparticle diffusion is considered as the rate-controlling step. However, if the straight line does not pass through the origin, this indicates that there is a difference in the mass transfer rate in the initial and final steps of adsorption, and diffusion is simultaneously involved. In summary, the intraparticle diffusion model suggests that both can be considered as rate-controlling steps.

2.2.3. Impact of Adsorbent Dose

Figure 3a,b show the effect of varying the adsorbent dose from 1 to 8 mg on the removal efficiency and adsorption capacity at pH = 9 and t = 20 min. The removal efficiency increased from 96% to 99% when the adsorbent dose was increased from 1 mg to 5 mg. The increase in the number of available active sites and the total surface area for Pb (II) ions removal are responsible for the increase in the removal efficiency.[67] From these experiments, we concluded that for an adsorbent dose of 5 mg, the removal efficiency reaches its optimal value, and a further increase of the adsorbent dose does not result in any appreciable change within the experimental error. Therefore, 5 mg was selected as the optimal adsorbent dose for the subsequent experiments.

2.2.4. Impact of Initial Concentration of Pb (II)

The effect of the initial concentration of Pb (II) in the range of 50 to 210 mg L^{-1} was investigated for the optimal conditions (pH = 9, time = 20 min, and adsorbent dose = 5 mg). As seen in Figure 3c,d, when the concentration of Pb (II) is 50 mg L^{-1}, the adsorption efficiency reaches 99%. This may be due to the increased attraction between the Pb (II) ions and the adsorbent. Since there are many active sites on the adsorbent surface, when the initial concentration of Pb (II) increases, the occupancy rate of active sites for Pb (II) ions gradually decreases until it reaches an almost saturated state. As the amount of adsorbent remains constant while the concentration of Pb (II) increases, the Pb (II) removal efficiency decreases.[68] However, at a high concentration of 210 mg L^{-1}, a remarkable q value of 566 mg g^{-1} was obtained, while the R value remained as high as 90%.

For a detailed study, two concentrations of 50 mg L^{-1} and 210 mg L^{-1} were selected for XRD, XPS, and magnetic measurements. Results of the XPS measurements have been discussed before. The XRD patterns (Figure 3e) show the presence of hydrocerussite ($Pb_3(CO_3)_2(OH)_2$) diffraction peaks (standard card 96-901-1389) indicating the formation of Pb (II) bond with carbon for both concentrations. These results suggest that Pb (II) forms a deposit for these concentrations through chemical adsorption on the adsorbent surface.[69] Room temperature field dependence of magnetization of the nanocomposite after adsorption were investigated for the selected concentrations, as shown in Figure 3f. As discussed before, with the increase of Pb (II) concentration, M_S reduces compared to the M_S value before adsorption to 12 Am^2 kg^{-1} and 10 Am^2 kg^{-1} for the concentrations of 50 ppm and 210 ppm, respectively.

2.2.5. Adsorption Isotherms

Despite the authors recognizing the criticality of this investigation, Langmuir, Freundlich, and Temkin models were used to study the linear regression of the adsorption isotherms. These three models are the most important and widely used isotherms used to describe adsorption processes. The Langmuir model states that a monomolecular layer is formed when adsorption occurs without interactions.[70] The Freundlich model considers active sites and a heterogeneous adsorption surface with different energies.[71] The Temkin isotherm model assumes a uniform distribution of binding energy.[72] **Figure** 4a-c show the fits obtained using the Langmuir, Freundlich, and Temkin isotherms, respectively. The governing linear equations are provided in the Supporting Information, and the obtained adsorption equilibrium constants are presented in Table 1. The values of correlation coefficients (R^2) obtained for the Langmuir, Freundlich, and Temkin

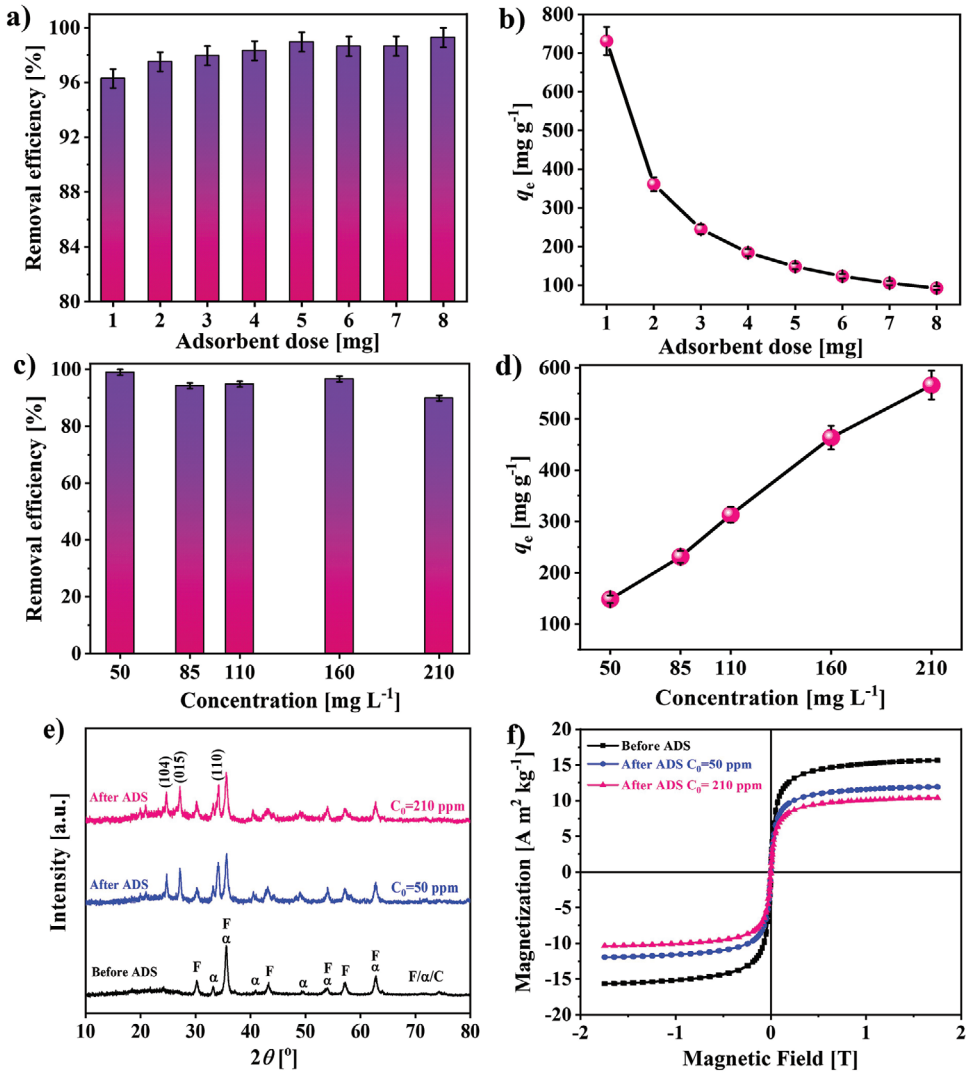

Figure 3. Effect of F/α/C adsorbent dose on a) removal efficiency and b) adsorption capacity. Effect of initial Pb (II) concentration on c) removal efficiency and d) adsorption capacity. e) XRD patterns showing peaks corresponding to Fe_3O_4 and α-Fe_2O_3 marked as "F" and "α", respectively, and f) Magnetic hysteresis loops of F/α/C nanocomposite before and after adsorption of Pb (II) for initial Pb (II) concentrations of 50 mg L^{-1} and 210 mg L^{-1}.

models are 0.94, 0.92, and 0.83, respectively. Based on these values, we conclude that the biosorption of Pb (II) on the nanocomposite as defined by the Langmuir linear model describes the adsorption mechanism most accurately. Nevertheless, we explored also the nonlinear regression method, which is a more general method used to estimate the parameters of the models.

To investigate the non-linear regression, Langmuir,[73] Freundlich,[74] Sips,[75] Temkin,[76] and Redlich-Peterson[77] isotherm models were considered (Figure 4d). The R^2 values have been calculated and listed in **Table 2** to compare the results and describe the biosorption process. As described earlier, the Langmuir model is based on a monolayer coating of particles on the surface of the adsorbent. The Freundlich model describes the coverage of several layers of particles on a heterogeneous adsorbent surface. Therefore, the Freundlich isotherm can describe the adsorption sites with 50% occupation of active sites. In addition to the previous models, Sips and Redlich-Peterson models were used for the transition range between the Langmuir and Freundlich models. The Temkin model assumes that the adsorption is a multi-layered process that decreases linearly with increasing coverage of the adsorption sites.[78] The best model for our data was selected by non-linear optimization fitting of the data. As seen in Figure 4d, the Temkin model has poor compatibility with the experimental data, as confirmed by its lowest R^2 value (0.72376). The four other models (Langmuir, Freundlich, Sips, and Redlich-Peterson) agree reasonably well with the experimental data, with R^2 values ranging between 0.91030 and 0.94527. The highest R^2 value (0.94527) corresponds to the Langmuir model, followed by the Redlich-Peterson model, which proves that the adsorbent surface is a combination of homogeneous and heterogeneous adsorption sites. However, since the Langmuir model shows the best fit to the experimental data, we can conclude that the surface has more homogeneous adsorption sites than heterogeneous sites.[79]

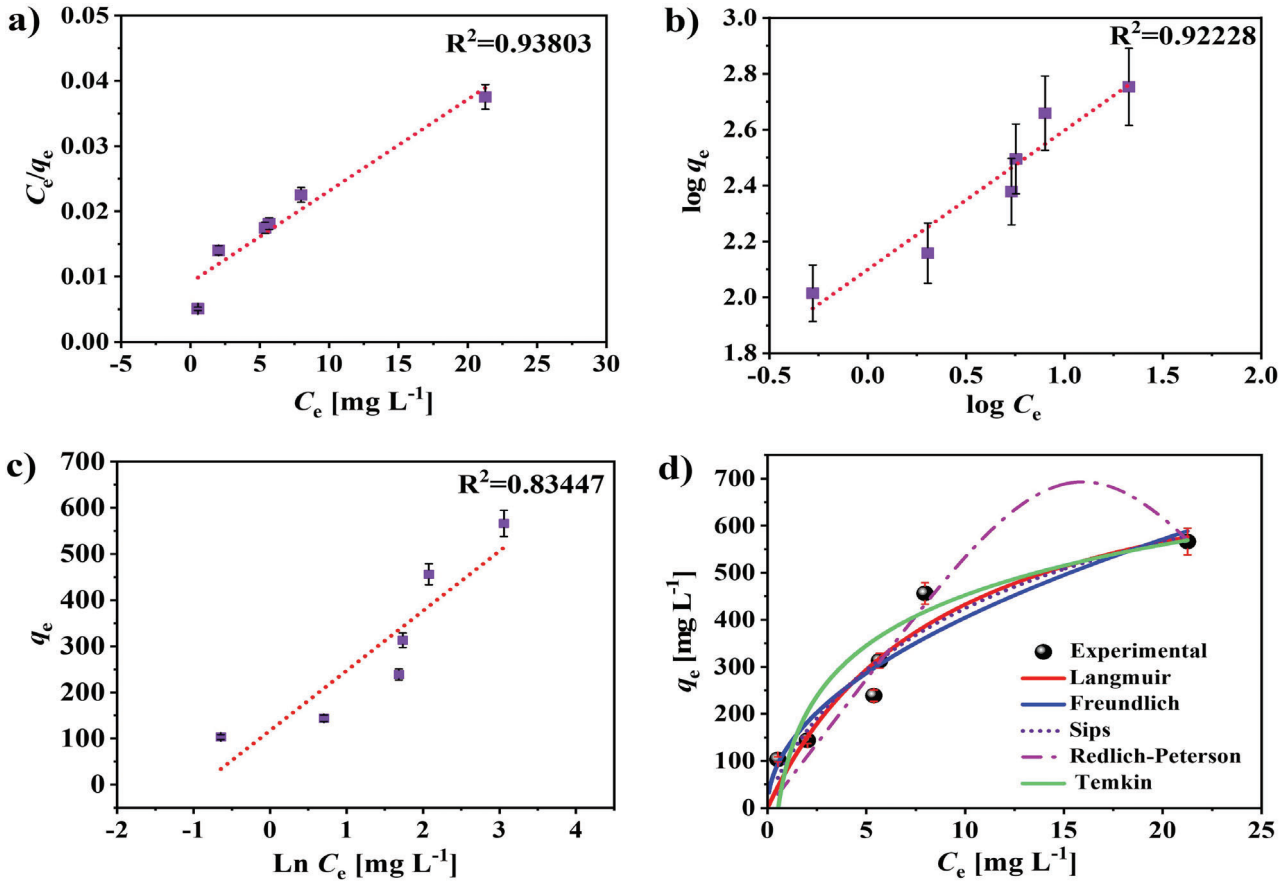

Figure 4. Linear fitting of Pb (II) adsorption data using a) Langmuir, b) Freundlich, and c) Temkin isotherm models. d) Nonlinear fitting using different isotherms.

2.2.6. Impact of Temperature and Thermodynamics

The effect of temperature on Pb (II) adsorption using the F/α/C nanocomposite is shown in **Figure** 5a,b. The effect of temperature was investigated in a temperature range of 306 K – 336 K, under pH = 9, time = 20 min, adsorbent dose = 5 mg, and initial Pb (II) concentration = 50 mg L^{-1}. As seen in Figure 5a, the removal efficiency increased from 99% to 100% with increasing temperature. The mobility of ions increases with increasing temperature, creating higher probability of interactions with the active sites.[80] Since it is not cost-effective to increase the temperature too much, therefore, the temperature of 326 K (adsorption capacity = 149 mg g^{-1}) was chosen as the optimal working temperature. To investigate the adsorption process, thermodynamic parameters including ΔH, ΔG, and ΔS of Pb (II) adsorption by the F/α/C nanocomposite were investigated (Figure 5c). The spontaneity of the adsorption process was examined (more details provided in the supporting information), and the results are presented in **Table** 3. Our results show that the value of ΔH is positive, which indicates that the adsorption process is endothermic and chemical. The value of ΔS is also positive and indicates an increase in the adsorption of Pb (II) ions at the solid-liquid interface. The calculated negative values of ΔG at the different temperatures indicate that the adsorption occurs as a spontaneous process.[81]

Table 2. Obtained parameters and correlation coefficients using different nonlinear fitting isotherm models for adsorption of Pb (II) by F/α/C nanocomposite.

Nonlinear Isotherm Model	Parameters	R^2
Langmuir	q_m [mg g^{-1}] = 818 (15)[a)] K_L [L mg^{-1}] = 0.11 (4)	0.94527
Freundlich	K_F [L mg^{-1}] = 128 (3) n = 0.50 (9)	0.91030
Sips	q_m [mg g^{-1}] = 911 (48) K_S [L mg^{-1}] = 0.06 (1) n = 0.76 (5)	0.92235
Temkin	b [J mol^{-1}] = 1.9 (2) A_T [L mg^{-1}] = 154 (4)	0.72376
Redlich-Peterson	K_{RP} [L mg^{-1}] = 54.8 (1) a_{RP} [L mg^{-1}] = 4.047 (3) g = 0.207	0.93626

[a)] Uncertainties in the last digit are given in parentheses.

2.2.7. Recovery and Reusability of the Adsorbent

Reusability of the adsorbent after removing heavy metals is a critical parameter to evaluate in any water treatment process via

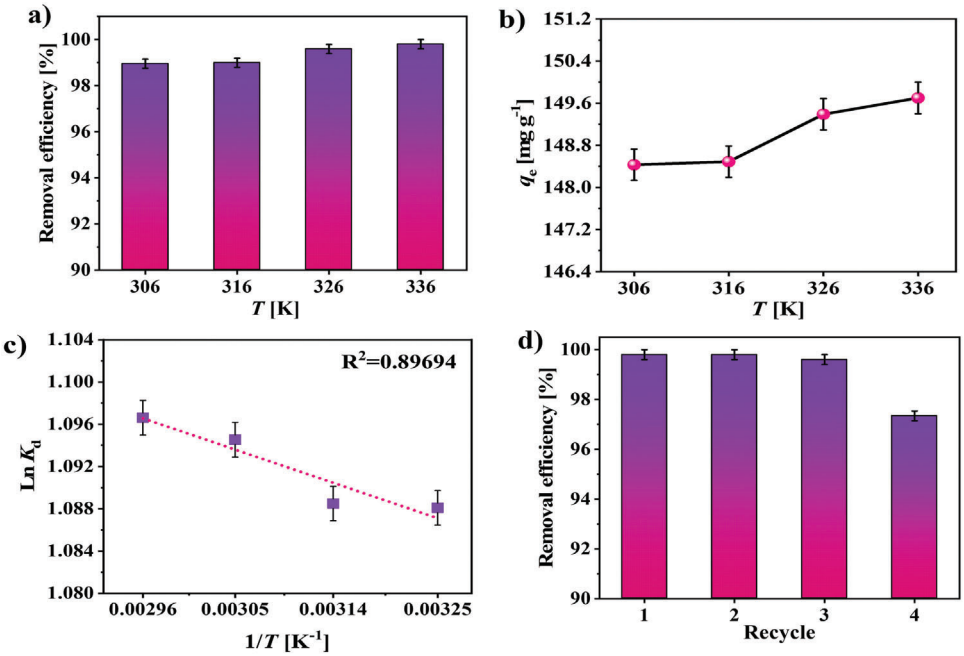

Figure 5. Effect of temperature on Pb (II) a) removal efficiency, and b) adsorption capacity by F/α/C nanocomposite. c) Plot of ln K_d versus 1/T, and d) reusability of F/α/C adsorbent for bath experiments.

adsorption. Reusability of the adsorbent implies that the entire process becomes more cost-effective. In this work, the adsorbents were regenerated by washing first with 0.1 M hydrochloric acid, followed by deionized water till neutral pH values were achieved. As seen in Figure 5d, the nanocomposite maintained its adsorption capacity with minor changes even for three cycles. In the fourth cycle, the adsorption efficiency decreased marginally to 97%. These experiments demonstrate the reusability of the nanoadsorbent for removing Pb (II) ions from contaminated water. In comparison to previous studies (listed in Table S2, Supporting Information), the F/α/C nanocomposite demonstrates significant adsorption capacity with a small adsorbent dose and low contact time, while maintaining its properties for four cycles.

3. Mechanism of Adsorption

Apple tree roots consist of a chemical composition and functional groups that can adsorb heavy metals from the soil, which also make them a promising adsorbent for the removal of heavy metal ions from water. During pyrolysis under nitrogen gas, the pore volume and surface area are increased, obtaining optimal textural properties for Pb(II) adsorption. The mechanism of adsorption of heavy metals is governed by two main phenomena: physical and chemical adsorption. Physical adsorption is mediated by surface adsorption and van der Waals forces, which create a weak force between the adsorbent and heavy metals.[82] Chemical adsorption is due to chemical bonding and leads to much stronger interaction between the adsorbent and ions.[83] **Figure 6** summarizes the different processes occurring during the adsorption of Pb (II) by the nanocomposite. The carbon surface contains hydroxyl and carboxyl groups that can form metal complexes with heavy metal ions in water, enabling surface adsorption. Chemical bonding and diffusion of heavy metal ions inside the carbon cavities are the main factors influencing the adsorption process. In addition, electrostatic attraction leads to the formation of ionic bonds.[84,85]

Electrostatic adsorption is strongly influenced by the pH of the solution. Increasing the concentration of OH in the aqueous solution affects the functional groups such as COOH and OH, so that they can adsorb cationic pollutants.[86] However, increasing the concentration of metal ions on the carbon surface disrupts the Pb (II) adsorption mechanism. Activated carbon contains functional groups such as OH and CO_3 that react with heavy metal ions and cause precipitation.[87] This has been seen in the XRD patterns of the nanocomposite after adsorption at pH = 9.

In the present study, Pb (II) adsorption and its dependence on pH have been explored. The XRD results showed that in acidic conditions, ions are electrostatically adsorbed, while in alkaline conditions, the results indicate the binding of metals on Fe_3O_4/α-Fe_2O_3/carbon adsorbent as oxides and hydroxides. Then, OH^- reacts with Fe (II), Fe (III), and Pb (II) in the solution forming precipitates of the respective hydroxides. Due to instability, Fe(OH) is reduced to FeO.[88,89] Finally, lead ions can be attached to additional adsorption sites through this process. These groups interact electrostatically with Pb (II) and $Pb(OH)_2$, and at higher

Table 3. Thermodynamic parameters of Pb (II) adsorption by F/α/C nanocomposite.

T [K]	K_q	ΔG [kJ mol^{-1}]	ΔH [kJ mol^{-1}]	ΔS [J K^{-1} mol^{-1}]	R^2
306	2.969	−2.786			
316	2.970	−2.878			
326	2.988	−2.985	0.27 (8)[a)]	9.92 (2)	0.89694
336	2.994	−3.082			

[a)] Uncertainties in the last digit are given in parentheses.

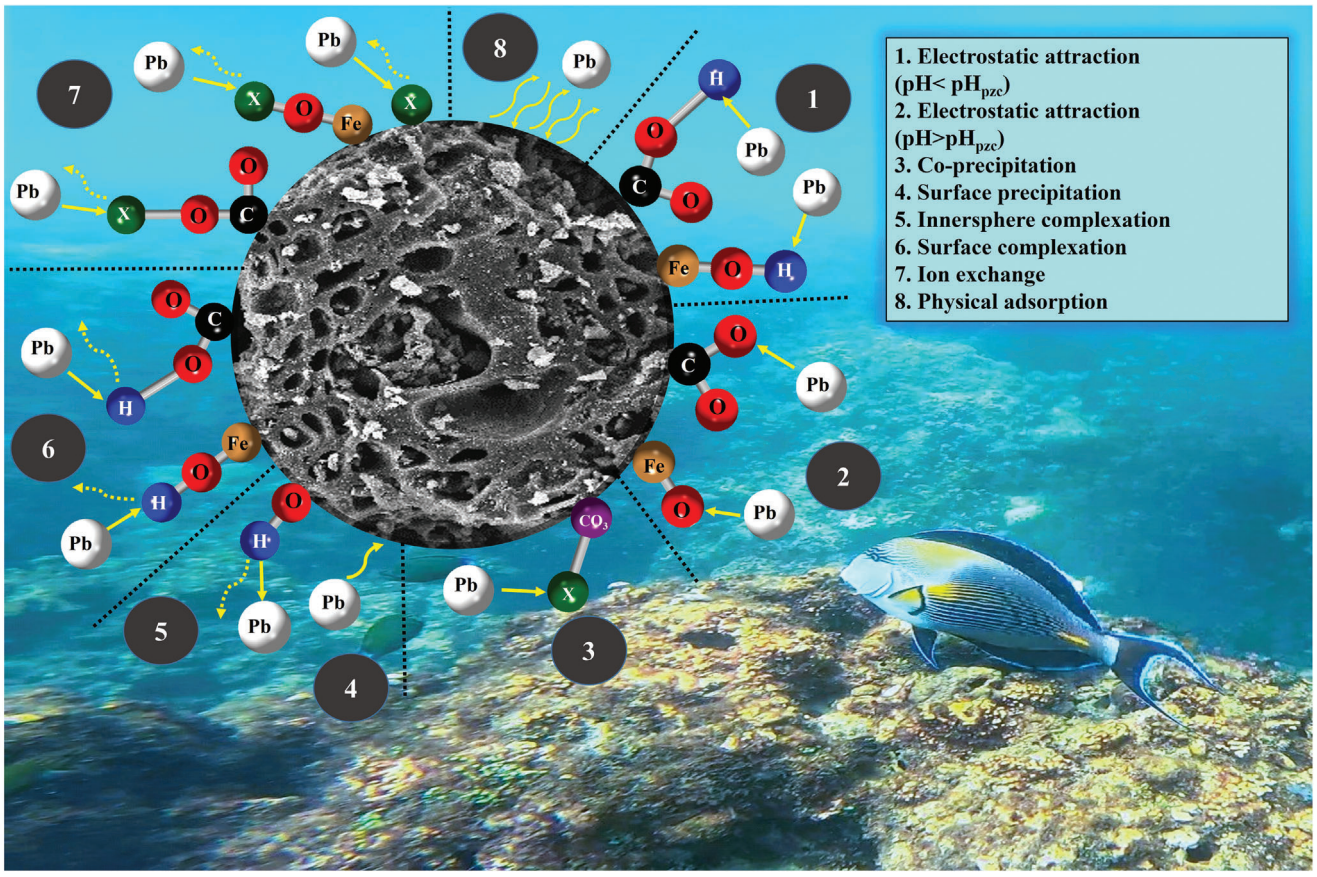

Figure 6. Main adsorption mechanisms for Pb (II) removal.

pH, Pb (II) hydroxides are deposited on the surface of the adsorbent. XPS results also confirm the adsorption of Pb (II) by the Pb-O group in hydrocerussite, suggesting that the lead adsorbed on the adsorbent surfaces probably exists in the form of Pb-R (R = CO, COO functional groups).

4. Microwave Absorption

After a comprehensive study of the water remediation capacity of the synthesized nanocomposite, we now explore its properties as a microwave absorber. For this, it is necessary to look at the relative complex permittivity ($\varepsilon_r = \varepsilon' - j\varepsilon''$) and relative complex permeability ($\mu_r = \mu' - j\mu''$) in the relevant frequency range of 8.2 GHz – 18 GHz. The real part of permittivity and permeability represent the storage of electric and magnetic energy, whereas the imaginary parts represent the energy dissipation within the material.[36] As seen in **Figure** 7a, the real and imaginary part of the dielectric permittivity vary from 2.83 to 3.02 and 0.11 to 0.22, respectively. Although the values of ε' and ε'' of the nanocomposite do not show any significant change in the measured frequency range, two peaks are observed at ≈12.02 GHz and 16.69 GHz. These peaks indicate a specific polarization relaxation process occurring at these frequencies. Iron oxide nanoparticles distributed on activated carbon increase surface polarization and create active interfaces on porous carbon. The porous structure traps air, which polarizes the interfaces with the material since air has a different dielectric property compared to the nanocomposite.

Figure 7b shows the variation of μ' and μ'' in the frequency range of 8.2 GHz -18 GHz. The real and imaginary parts of the complex permeability range from 0.98 to 1.02 and −0.00014 to 0.017, respectively. Several peaks are observed for the complex permeability of the sample, which is related to natural resonance and loss of exchange resonance.[90] The values of μ' and μ'' are close to one and zero, respectively, indicating negligible magnetic losses. Furthermore, the negative μ'' values indicate the radiation of magnetic energy without any absorption.[91]

Dielectric loss ($\tan \delta_\varepsilon = \varepsilon''/\varepsilon'$) and magnetic loss ($\tan \delta_\mu = \mu''/\mu'$) values are presented in Figure 7c. The amount of dielectric loss is mainly determined by the loss of electrical conductivity and polar relaxation. When the EMW enters the absorber, the charge carriers create a current through the electric field. Therefore, electrical energy is converted into thermal energy and dissipated. Besides this, if the conductivity is high, the number of wave collisions and reflections increases, which ultimately causes impedance mismatch and weakening of EMWs.[92,93] Comparing the values of dielectric loss and magnetic loss, the dielectric loss tangent is greater than the magnetic loss tangent. Therefore, the contribution of dielectric loss is more substantial.

The measured electromagnetic parameters not only affect the impedance matching but also determine its attenuation

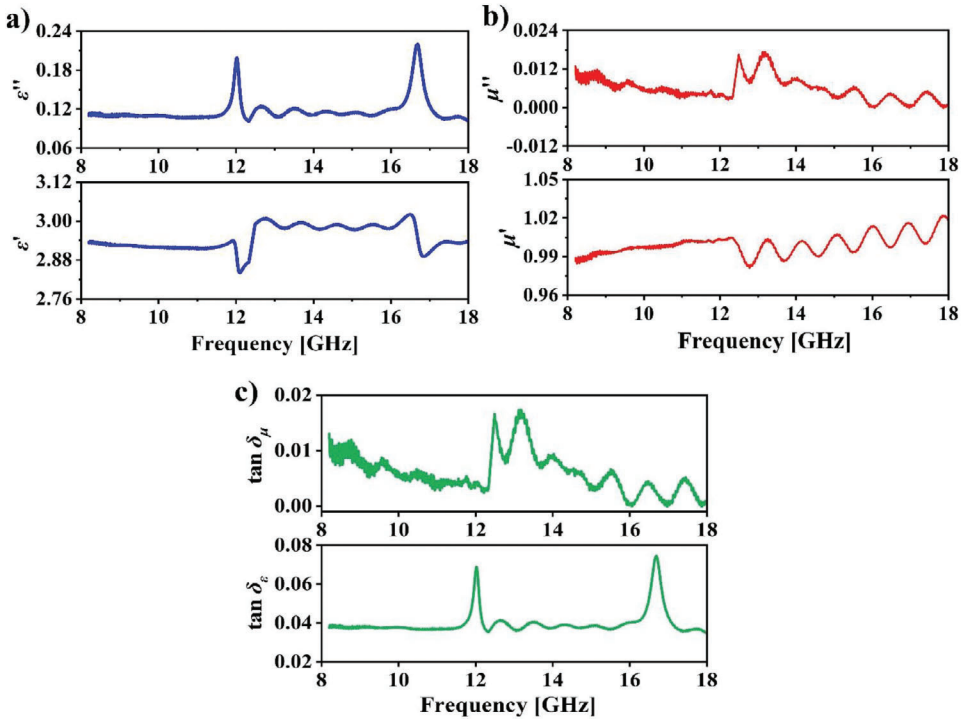

Figure 7. a) Frequency dependence of the real and imaginary parts of relative complex permittivity, b) frequency dependence of the real and imaginary parts of relative complex permeability, c) dielectric loss tangent, and d) magnetic loss tangent for F/α/C nanocomposite.

capability. To evaluate the absorption of EMWs, the amount of reflection loss is calculated by the transmission line theory:[94]

$$RL = 20\log\left|\frac{Z_{in} - Z_0}{Z_{in} + Z_0}\right| \quad (1)$$

$$Z_{in} = Z_0\sqrt{\frac{\mu_r}{\varepsilon_r}}\tanh\left(j\frac{2\pi fd}{c}\sqrt{\mu_r\varepsilon_r}\right) \quad (2)$$

where, RL is the reflection loss, Z_0 is the impedance of free space (equivalent to 377 Ω), Z_{in} is the input impedance, f is the frequency of the EMW, d is the thickness of the absorbing material, and c is the speed of light in vacuum. An RL value less than −10 dB indicates good absorption of EMWs, and the corresponding frequency range represents the effective absorption bandwidth.[95] The two-dimensional and three-dimensional representations of the frequency and thickness dependence of the RL are presented in **Figure 8**a,b, where the frequency is varied between 8.2 GHz −18 GHz and the thickness of the sample varies between 1.5 mm and 4.5 mm. A comparison of the RL values for four sample thicknesses shows that the best microwave absorption performance is achieved for the sample thickness of 4.5 mm. At this thickness (4.5 mm), the RL value reaches −75.2 dB at 15.2 GHz, and the effective absorption bandwidth is 8.3 GHz. In contrast, for a slightly thinner sample (3.5 mm), the effective absorption bandwidth decreases to 7.8 GHz with an RL value of −61.7 dB at a frequency of 16.3 GHz.

In addition to magnetic and dielectric losses, impedance matching between the material and free space (Z_{in}/Z_0) is an important factor in microwave absorption.[96] The matching curves of impedance versus frequency for thicknesses of 1.5 mm to 4.5 mm are shown in Figure 8c,d. Ideal impedance matching occurs when Z_{in}/Z_0 is equal to or close to 1. When impedance is matched, EMWs can enter the material without reflection. It is evident that the impedance matching value of the composite at the thicknesses of 3.5 mm and 4.5 mm is much closer to 1.0. Poor impedance matching will result in insufficient absorption capability.

Polar relaxation losses can arise from ionic, electronic, and/or surface dipole polarization.[97] Ionic polarization is caused by the relative movements of cations and anions, while electronic polarization occurs as a result of the movement of electrons relative to the nucleus. Dipole polarization is caused by the rotation of the dipole moment in the direction of the electric field and affects the dielectric loss. Relaxation loss is evaluated by the Debye equation:[98]

$$\left(\varepsilon' - \frac{\varepsilon_s + \varepsilon_\infty}{2}\right)^2 + (\varepsilon'')^2 = \left(\frac{\varepsilon_s - \varepsilon_\infty}{2}\right)^2 \quad (3)$$

where, ε_s is the static dielectric constant, and ε_∞ is the dielectric constant at infinite frequency. **Figure 9**a shows the plot of ε'' versus ε', revealing the Cole-Cole semicircle arising from Equation 3. This indicates the presence of polarization relaxation processes.[99,100] The Cole-Cole plot exhibits two semicircles, which shows that the dielectric loss mechanism is high and causes the weakening of EMWs. The large radius of the Cole-Cole semicircles may be related to the carbonization temperature.[101]

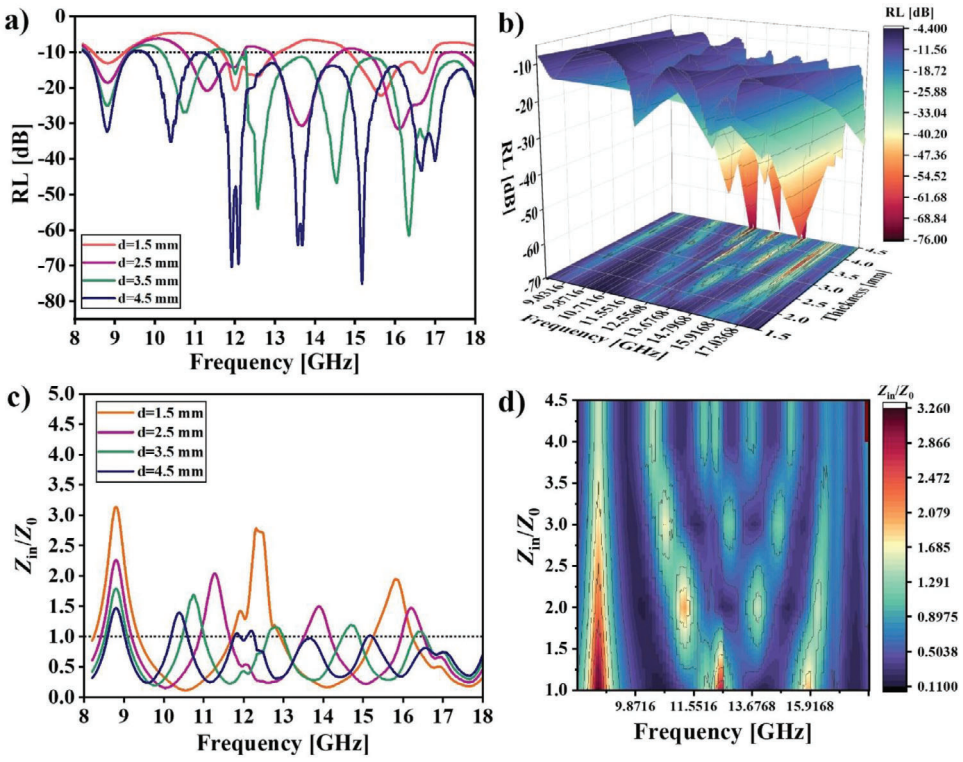

Figure 8. a) Reflection loss in the frequency range 8.2 GHz – 18 GHz and b) corresponding 3-D contour map for different thicknesses of F/α/C nanocomposite. c) Impedance matching and d) 2-D mapping plots of Z_{in}/Z_0 value in the frequency range 8.2 GHz – 18 GHz.

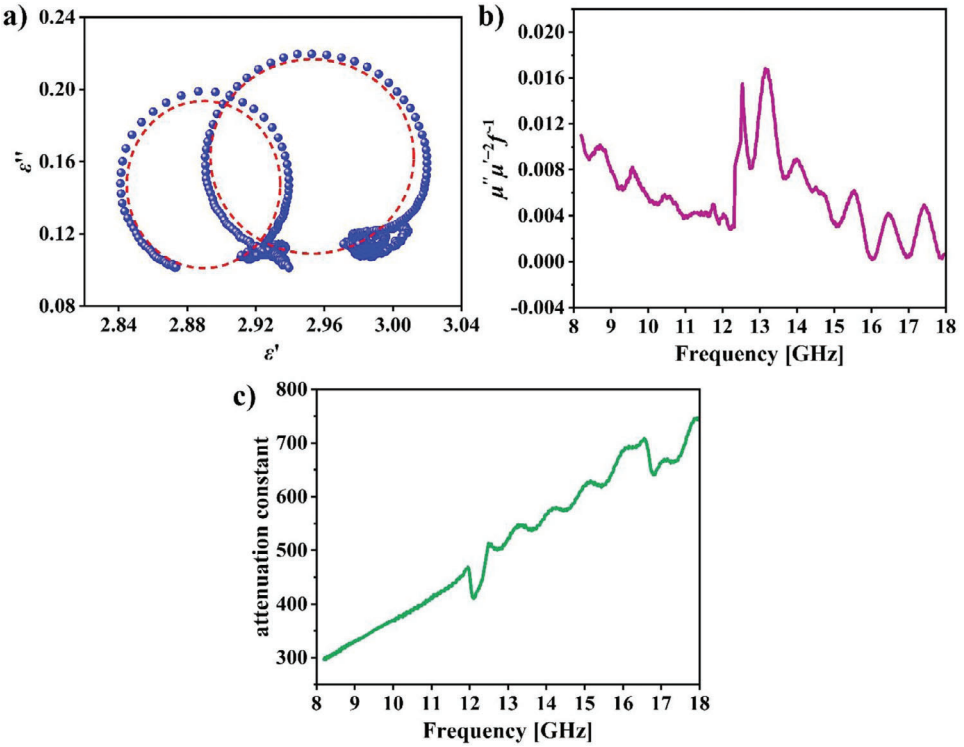

Figure 9. a) Cole-Cole plot; Frequency dependence of b) $C_0 = \mu''\mu'^{-2} f^{-1}$, and c) attenuation constant for F/α/C nanocomposite.

Magnetic losses are generally related to exchange resonance, natural resonance, and eddy current losses. The amount of eddy current loss can be obtained from the following relationship:[102]

$$C_0 = \mu'' \, \mu'^{-2} f^{-1} \tag{4}$$

According to the skin effect theory, if the value of C_0 remains unchanged, the magnetic loss is affected only by the eddy current loss. Figure 9b shows the variation of C_0 for the F/α/C nanocomposite in the frequency range of 8.2 GHz -18 GHz. The value of C_0 is not constant with frequency. Therefore, in this sample, there is a possibility of natural resonance and exchange resonance, which play a fundamental role in the absorption of EMWs.

One of the characteristics of wave behavior is the attenuation of EMW propagation. The following relationship is used to measure the damping or attenuation constant (α) utilizing the transmission theory of EMWs:[102]

$$\alpha = \frac{\sqrt{2}\pi f}{c} \sqrt{(\mu''\varepsilon'' - \mu'\varepsilon') + \sqrt{(\mu''\varepsilon'' - \mu'\varepsilon')^2 + (\mu'\varepsilon'' + \mu''\varepsilon)'^2}} \tag{5}$$

As seen in Figure 9c, α shows a general increasing trend with increasing frequency, with its value increasing steadily from 300.55 to 746.16 in the frequency range 8.2 GHz – 18 GHz. Thus, the nanocomposite possesses an excellent attenuation capability to dissipate the energy of electromagnetic waves.

The nanocomposite used in this work exhibits a reflection loss of −75.22 dB for a thickness of 4.5 mm with a wide effective absorption bandwidth in the frequency range 8.2 GHz – 18 GHz. The possible mechanism of absorption of EMWs can be attributed to the highly porous structure of the nanocomposite. When EMWs hit the surface of a material, some of the reflected waves are scattered by the incident waves. The nanocomposite contains large number of pores, so that when an EMW falls on it, it suffers multiple internal reflections and gets scattered. This increases the effective propagation path of the EMW inside the material thereby improving absorption. The biocarbon structure has an interconnected conductive network that can convert EMW energy into current. Interfaces in composites can create heterogeneous load distribution at the interface. Since magnetite and hematite are magnetic, the EMW creates an eddy current through the material. Therefore, the F/α/C nanocomposite shows good absorption performance due to ideal impedance matching and synergistic effect between different attenuation mechanisms. The obtained RL values are on par or even better than some of the reported EMW absorbers in literature (Table S3, Supporting Information).

5. Conclusion

In this study, Pb (II) ion removal from aqueous solution was investigated using a new triphasic F/α/C nanocomposite. The results of FESEM, EDS/mapping, FTIR, Raman, XRD, BET, VSM, and XPS analyses confirmed a successful synthesis of the composite, and subsequent adsorption experiments proved its effectiveness in Pb (II) removal. The optimal values of pH, contact time, adsorbent dose, initial concentration, and temperature were found to be 9, 20 min, 5 mg, 50 mg L^{-1}, and 326 K, respectively. Reusability tests showed that the nanocomposite can be regenerated and used for multiple cycles while maintaining its high adsorption efficiency. Apart from a high adsorption capacity and the possibility of rapid magnetic separation of the pollutants post-adsorption, the synthesized nanocomposite has the advantages of non-toxicity, low cost, and biocompatibility. The porous structure of activated carbon also results in high microwave absorption efficiency with an RL value of −75.2 dB and a wide absorption bandwidth of 8.3 GHz at thickness of 4.5 mm. The material shows good band tunability with the possibility of controlling the absorption properties by changing the thickness of the absorbing layer. Overall, the reported multifunctional triphasic nanocomposite has great potential to contribute towards clean water availability and electromagnetic pollution (SDGs 6 and 13).

6. Experimental Section

Materials and Chemicals: For the synthesis of the magnetic compounds, iron chloride metal salts ($FeCl_2.4H_2O$: $FeCl_3.6H_2O$, 99%) from Merck were used. The pH was adjusted using 0.1 M sodium hydroxide (NaOH, 99%) and 0.1 M hydrochloric acid (HCl, 37%). For biomass activation and to determine the point of zero charge (pH_{pzc}), zinc chloride ($ZnCl_2$, 99%) and 0.1 M lead nitrate ($PbNO_3$, 99%) (both from Merck), respectively, were used. Lead nitrate was used to prepare Pb (II) solution for bath experiments.

Fabrication of F/α/C: As reported in previous works, iron oxide/carbon nanocomposites were prepared using co-precipitation method.[103,104] The roots of the apple trees were washed with deionized water several times. After drying, the roots were cut into small pieces and soaked in zinc chloride overnight. After draining the excess water, the wood was dried at 110 °C for 3 h. Finally, it was pyrolyzed in a furnace under nitrogen gas flow at 600 °C for 1 h. The obtained activated carbon was soaked in 10% hydrochloric acid for 24 h, and subsequently washed with deionized water until the pH of the water reached ≈7. The powders were then dried in an oven at 90 °C for 1 h. Finally, 70 and 100-micron meshes were used to obtain homogeneous powder.

For anchoring MNPs on the carbon, the metal salts were dissolved in 50 mL of deionized water and the temperature was raised to 80 °C. After stirring for 30 min, activated carbon was added to the salt solution, followed by 15 min stirring. Next, sodium hydroxide solution was added to precipitate the solution and it was allowed to stand for 30 min for it to settle well. Finally, the precipitate was separated using a NdFeB magnet.

To form a layer of hematite on magnetite particles, the obtained black powder was heated at 100 °C for 30 min, till its color turned brownish/reddish. The synthesis process of F/α/C magnetic nanocomposite is shown schematically in Figure S1 (Supporting Information). To study the microwave absorption characteristics, the prepared powder sample was mixed with paraffin wax with 30% weight ratio and pressed in the form of rectangular pellets. No further annealing was performed on the pellets.

Characterization Techniques: FTIR spectra were obtained using a TENSOR 27 spectrometer. XRD patterns and Raman spectra were obtained using a Siemens D5000 and Horiba Jobin-Yvon Labram HR800 (excitation wavelength: 532 nm), respectively. For recording the XRD patterns, a scan rate of 1°/min and step size of 0.02° (in the 2θ range of 20°–80°) were employed. To study the morphology and elemental composition of the samples, an FESEM (MIRA3-TESCAN) and a Zeiss LEO 1550 SEM equipped with EDS, respectively, were used. Specific surface area and pore characteristics (i.e., size and size distribution) of the samples was studied by BET method via nitrogen adsorption-desorption measurements using a BELSORP Mini II analyzer. In this method, a complete layer of adsorbed molecules is created on the surface. From the average thickness of a molecule, it is possible to calculate the surface area occupied by a

molecule and measure the total surface area of the sample based on the amount of adsorbed substance.

A Lakeshore model 4701 VSM with maximum field of 1.8 T was used to record room temperature field dependence of magnetization curves of the adsorbent. To further study the elemental composition and adsorption mechanism, a PHI QUANTERA II XPS with Al K-alpha source was used. The XPS spectra were fitted using Kol Software. All spectra were fitted using a Shirley background plus Voigt functions except the main C 1s peak for which a Doniach Sunich lineshape was used. For bath experiments and to determine the Pb (II) ions concentration in the solutions, an ICP 5000 DV inductively coupled plasma optical emission spectrometer was used. The measurements were repeated three times and the spread in results were used to indicate the corresponding errors in the removal efficiency and adsorption capacity.

The EMW absorption properties in the X (8.2 – 12.4 GHz) and Ku (12.4 – 18 GHz) bands were analyzed using a Keysight N5227A PNA network analyzer. The network analyzer was calibrated in the Transmission Line mode using mechanical calibration kits: Keysight N9911X-WR90 (X band) and Keysight N9911X-WR62 (Ku band). The pellets were fitted inside the rectangular waveguides and the complex permeability and permittivity were obtained by the Nicolson – Ross – Weir Method using Keysight N1500A Materials Measurement Suite (2020).

Bath Experiments and Pb (II) Ions Removal Studies: The effect of different parameters, including pH, contact time, adsorbent dose, initial Pb (II) concentration, and temperature, were studied to find the optimal conditions for Pb (II) removal. During the pH experiments, the pH of the Pb (II) solution was adjusted using diluted hydrochloric acid and sodium hydroxide solution. All adsorption studies using the F/α/C nanocomposite were performed for a predetermined time. After adsorption, the adsorbent was recovered from the solution containing lead using a neodymium magnet, and the concentration of Pb (II) ions in water was measured. The removal efficiency (R) and adsorption capacity (q) were calculated using Equations 6 and 7.

$$R\ (\%) = \left(\frac{C_i - C_e}{C_i}\right) \times 100 \tag{6}$$

$$q = \left(\frac{C_i - C_e}{m}\right) \times V \tag{7}$$

where, C_i is the initial concentration of lead in the solution (mg L^{-1}), C_e is the final concentration of ions after adsorption (mg L^{-1}), m is the mass of the adsorbent (g), and V is the volume of the solution containing lead (L). The obtained data were analyzed using adsorption kinetics, linear and non-linear models, and thermodynamics.

Supporting Information

Supporting Information is available from the Wiley Online Library or from the author.

Acknowledgements

The authors gratefully acknowledge funding from the ÅForsk Foundation (grant number 21–231), Stiftelsen Olle Engkvist Byggmästare (grant number 214–0346), and the Swedish Research Council (grant number 2021–03675). The authors also acknowledge the support of the "Network 4 Energy Sustainable Transition-NEST" project (code PE0000021), adopted by "Ministero dell'Universita e della Ricerca (MUR)," according to attachment E of Decree No. 1561/2022.

Conflict of Interest

The authors declare no conflict of interest.

Data Availability Statement

The data that support the findings of this study are available from the corresponding author upon reasonable request.

Keywords

activated carbon, electromagnetic wave absorption, magnetism, nanocomposite, Pb (II) ions adsorption

Received: July 29, 2024
Revised: September 2, 2024
Published online:

[1] A. Fleming, R. M. Wise, H. Hansen, L. Sams, *Marine Policy* **2017**, *86*, 94.
[2] F. N. Chaudhry, M. Malik, *J. Ecosyst. Ecography* **2017**, *7*, 225.
[3] G. Redlarski, B. Lewczuk, A. Żak, A. Koncicki, M. Krawczuk, J. Piechocki, K. Jakubiuk, P. Tojza, J. Jaworski, D. Ambroziak, *Biomed Res. Int.* **2015**, *2015*, 234098.
[4] A. Ahlbom, M. Feychting, *Br. Med. Bull.* **2003**, *68*, 157.
[5] B. Wang, J. Lan, C. Bo, B. Gong, J. Ou, *RSC Adv.* **2023**, *13*, 4275.
[6] T. G. Kazi, N. Jalbani, N. Kazi, M. K. Jamali, M. B. Arain, H. I. Afridi, A. Kandhro, Z. Pirzado, *Renal Failure* **2008**, *30*, 737.
[7] T. A. Salah, A. M. Mohammad, M. A. Hassan, B. E. El-Anadouli, *J. Taiwan Inst. Chem. Eng.* **2014**, *45*, 1571.
[8] N. Abdullah, N. Yusof, W. J. Lau, J. Jaafar, A. F. Ismail, *J. Ind. Eng. Chem.* **2019**, *76*, 17.
[9] G. Crini, E. Lichtfouse, *Environ. Chem. Lett.* **2019**, *17*, 145.
[10] M. E.-S. Abdel-Raouf, R. K. Farag, A. A. Farag, M. Keshawy, A. Abdel-Aziz, A. Hasan, *ACS Omega* **2023**, *8*, 10086.
[11] J. Khan, S. Lin, J. C. Nizeyimana, Y. Wu, Q. Wang, X. Liu, *J. Cleaner Prod.* **2021**, *319*, 128687.
[12] Y. Li, H. Yin, Y. Cai, H. Luo, C. Yan, Z. Dang, *Chemosphere* **2023**, *311*, 136976.
[13] K. R. Tolod, S. Hernández, E. A. Quadrelli, N. Russo, in *Studies in Surface Science and Catalysis*, Vol. *178* (Eds.: S. Albonetti, S. Perathoner, E. A. Quadrelli), Elsevier, New York **2019**, Ch. 4.
[14] C. Martinez-Boubeta, K. Simeonidis, in *Nanoscale Materials in Water Purification*, (Eds.: S. Thomas, D. Pasquini, S.-Y. Leu, D. A. Gopakumar), Elsevier, New York **2019**, Ch. p. 20.
[15] Z. Kheshti, K. Azodi Ghajar, A. Altaee, M. R. Kheshti, *Sep. Purif. Technol.* **2019**, *212*, 650.
[16] N. Kataria, V. K. Garg, *Chemosphere* **2018**, *208*, 818.
[17] M. Jain, V. Garg, K. Kadirvelu, *Bioresour. Technol.* **2013**, *129*, 242.
[18] N. Azouaou, Z. Sadaoui, A. Djaafri, H. Mokaddem, *J. Hazard. Mater.* **2010**, *184*, 126.
[19] V. Gupta, A. Nayak, *Chem. Eng. J.* **2012**, *180*, 81.
[20] R. Foroutan, S. J. Peighambardoust, S. H. Peighambardoust, M. Pateiro, J. M. Lorenzo, *Molecules* **2021**, *26*, 2241.
[21] R. Sudha, K. Latha, R. Jayalakshmi, *Indian J. Chem. Technol.* **2023**, *30*, 672.
[22] K. H. Kamal, M. Attia, N. S. Ammar, E. M. Abou-Taleb, *Inorg. Chem. Commun.* **2021**, *130*, 108742.
[23] M. Bagherzadeh, B. Aslibeiki, N. Arsalani, *Sci. Rep.* **2023**, *13*, 3960.
[24] M. Solkin, *Transportation Research Procedia* **2021**, *59*, 310.
[25] G. Schmitt, J. Brachmann, B. Waldecker, L. Navarrete, T. Beyer, A. Pfeifer, W. Kulber, *PACE* **1991**, *14*, 982.
[26] J. Paś, S. Duer, *Neural. Comput. Appl.* **2013**, *23*, 2143.
[27] A. Kocaman, G. Altun, A. A. Kaplan, Ö. G. Deniz, K. K. Yurt, S. Kaplan, *Environ. Res.* **2018**, *163*, 71.
[28] L. Hardell, M. Carlberg, *Int. J. Oncol.* **2019**, *54*, 111.

[29] S. S. Seker, O. Simsek, *Int. j. innov. res. sci. eng. technol.* **2022**, *11*, 14201.
[30] J. Li, D. Zhou, P. Wang, W. Liu, J. Su, *J. Mater. Chem. A* **2020**, *8*, 20337.
[31] S. Ni, S. Lin, Q. Pan, F. Yang, K. Huang, D. He, *J. Phys. D: Appl. Phys.* **2009**, *42*, 055004.
[32] J. Ji, Y. Huang, J. Yin, X. Zhao, X. Cheng, S. He, X. Li, J. He, J. Liu, *ACS Appl. Nano Mater* **2018**, *1*, 3935.
[33] X. Yan, T. Ji, W. Ye, *J. Nanomater.* **2020**, *2020*, 6980730.
[34] F. Ademiluyi, E. David-West, *Int. Scholarly Res. Not.* **2012**, *2012*, 674209.
[35] J. Zhang, H. Fu, X. Lv, J. Tang, X. Xu, *Biomass Bioenergy* **2011**, *35*, 464.
[36] Z. Wu, K. Tian, T. Huang, W. Hu, F. Xie, J. Wang, M. Su, L. Li, *ACS Appl. Mater. Interfaces* **2018**, *10*, 11108.
[37] M. Cagnasso, V. Boero, M. A. Franchini, J. Chorover, *Colloids Surf., B* **2010**, *76*, 456.
[38] M. M. Marchioretto, H. Bruning, W. Rulkens, *Sep. Sci. Technol.* **2005**, *40*, 3393.
[39] C. F. Carolin, P. S. Kumar, A. Saravanan, G. J. Joshiba, M. Naushad, *J. Environ. Chem. Eng.* **2017**, *5*, 2782.
[40] Z. Song, F. Lian, Z. Yu, L. Zhu, B. Xing, W. Qiu, *Chem. Eng. J.* **2014**, *242*, 36.
[41] R. Foroutan, R. Mohammadi, J. Razeghi, B. Ramavandi, *Algal Res.* **2019**, *40*, 101509.
[42] M. Khoshnam, J. Farahbakhsh, M. Zargar, A. W. Mohammad, A. Benamor, W. L. Ang, E. Mahmoudi, *Sci. Rep.* **2021**, *11*, 20378.
[43] M. Yegane Badi, A. Azari, H. Pasalari, A. Esrafili, M. Farzadkia, *J. Mol. Liq.* **2018**, *261*, 146.
[44] B. H. Jume, N. Valizadeh Dana, M. Rastin, E. Parandi, N. Darajeh, S. Rezania, *Molecules* **2022**, *27*, 8841.
[45] P. N. Chuc, N. Q. Bac, D. T. P. Thao, N. T. Kien, N. T. H. Chi, N. V. Noi, V. T. Nguyen, N. T. H. Bich, D. N. Nhiem, D. Q. Khieu, *Environ. Eng. Res.* **2024**, *29*, 230076.
[46] N. Karić, M. Vukčević, M. Maletić, S. Dimitrijević, M. Ristić, A. P. Grujić, K. Trivunac, *Int. J. Biol. Macromol.* **2023**, *241*, 124527.
[47] G. Qi, Z. Pan, X. Zhang, S. Chang, H. Wang, M. Wang, W. Xiang, B. Gao, *Environ. Res.* **2023**, *216*, 114732.
[48] M. Kaur, S. Kumari, P. Sharma, *Biotechnol. Rep.* **2020**, *25*, e00410.
[49] W. Liu, K. Li, X. Hu, X. Hu, R. Zhang, Q. Li, *fenvc* **2021**, *2*, 693509.
[50] A. Adeleke, A. Onifade, A. Sangoremi, A. Anifowose, O. Isola, B. Olawoye, *J. Appl. Sci. Environ. Manage.* **2023**, *27*, 919.
[51] A. Sánchez-Navas, O. López-Cruz, N. Velilla, I. Vidal, *J. Cryst. Growth* **2013**, *376*, 1.
[52] P. M. Kouotou, Z.-Y. Tian, *Proc. Combust. Inst.* **2019**, *37*, 5445.
[53] W. Ramadan, M. Kareem, B. Hannoyer, S. Saha, *Adv. Mater. Res.* **2011**, *324*, 129.
[54] A. Shahzad, B. Aslibeiki, S. Slimani, S. Ghosh, M. Vocciante, M. Grotti, A. Comite, D. Peddis, T. Sarkar, *Sci. Rep.* **2024**, *14*, 17674.
[55] Y. Liu, X. Liu, W. Dong, L. Zhang, Q. Kong, W. Wang, *Sci. Rep.* **2017**, *7*, 12437.
[56] S. L. Iconaru, R. Guégan, C. L. Popa, M. Motelica-Heino, C. S. Ciobanu, D. Predoi, *Appl. Clay Sci.* **2016**, *134*, 128.
[57] J. Gao, X. Wu, S. Qin, Y.-c. Li, *High Pressure Res* **2016**, *36*, 1.
[58] J. D. Pasteris, Y. Bae, D. E. Giammar, S. N. Dybing, C. H. Yoder, J. Zhao, Y. Hu, *Minerals* **2021**, *11*, 1047.
[59] N. A. Medellin-Castillo, E. Padilla-Ortega, M. C. Regules-Martínez, R. Leyva-Ramos, R. Ocampo-Pérez, C. Carranza-Alvarez, *Sustainable Environ. Res.* **2017**, *27*, 61.
[60] W. Zhang, H. Shiozawa, C. Wu, I. Hamerton, D. Cox, S. Silva, *J. Nanosci. Nanotechnol.* **2012**, *12*, 84.
[61] M. Stojkovska, R. Davi, G. Carraro, M. Smerieri, M. Lewandowski, M. Rocca, L. Vattuone, L. Savio, *Appl. Surf. Sci.* **2020**, *512*, 145774.
[62] B. Barzegar, S. J. Peighambardoust, H. Aghdasinia, R. Foroutan, *Environ. Sci.: Water Res. Technol.* **2023**, *9*, 3417.
[63] V. Nejadshafiee, M. R. Islami, *Mater. Sci. Eng. C.* **2019**, *101*, 42.
[64] E. D. Revellame, D. L. Fortela, W. Sharp, R. Hernandez, M. E. Zappi, *Clean. Eng. Technol.* **2020**, *1*, 100032.
[65] W. J. Weber, J. C. Morris, *J. Sanit. Eng. Div.* **1963**, *89*, 31.
[66] J. López-Luna, L. E. Ramírez-Montes, S. Martinez-Vargas, A. I. Martínez, O. F. Mijangos-Ricardez, M. d. C. A. González-Chávez, R. Carrillo-González, F. A. Solís-Domínguez, M. d. C. Cuevas-Díaz, V. Vázquez-Hipólito, *SN Appl. Sci.* **2019**, *1*, 950.
[67] K. K. Zadeh, D. Jafari, *Biomass Convers. Biorefin.* **2024**, *14*, 19025.
[68] J. Qi, H. Zhu, T. Yang, X. Wang, Z. Wang, X. Lei, B. Li, W. Qian, *Arabian J. Chem.* **2024**, *17*, 105411.
[69] W. Jin, Y. Yang, J. Jin, M. Xu, Z. Zhang, F. Dong, M. Shao, Y. Wan, *Environ. Sci. Pollut. Res.* **2024**, *31*, 43687.
[70] I. Langmuir, *J. Am. Chem. Soc.* **1916**, *38*, 2221.
[71] H. M. F. Freundlich, *J. Phys. chem* **1906**, *57*, 1100.
[72] M. J. Temkin, V. Pyzhev, *Acta Physiochim URSS* **1940**, *12*, 217.
[73] I. Langmuir, *J. Am. Chem. Soc.* **1918**, *40*, 1361.
[74] H. Freundlich, *Z. Phys. Chem.* **1907**, *57*, 385.
[75] R. Sips, *J. Chem. Phys.* **1948**, *16*, 490.
[76] M. Tempkin, V. Pyzhev, *Acta Phys. Chim. USSR* **1940**, *12*, 327.
[77] O. Redlich, D. L. Peterson, *J. Phys. Chem.* **1959**, *63*, 1024.
[78] I. W. Almanassra, V. Kochkodan, G. Mckay, M. A. Atieh, T. Al-Ansari, *J. Environ. Sci. Health, Part A* **2021**, *56*, 1206.
[79] K. V. Kumar, S. Gadipelli, B. Wood, K. A. Ramisetty, A. A. Stewart, C. A. Howard, D. J. Brett, F. Rodriguez-Reinoso, *J. Mater. Chem. A* **2019**, *7*, 10104.
[80] N. Erduran, Ö. Işılar, *Polym. Bull.* **2024**, *81*, 10933.
[81] A. Moradi, P. Najafi Moghadam, R. Hasanzadeh, M. Sillanpää, *RSC Adv.* **2017**, *7*, 433.
[82] F. S. Higashikawa, R. F. Conz, M. Colzato, C. E. P. Cerri, L. R. F. Alleoni, *J. Cleaner Prod.* **2016**, *137*, 965.
[83] F. He, B. Ma, C. Wang, Y. Chen, X. Hu, *Sep. Purif. Technol.* **2023**, *310*, 123234.
[84] M. I. Inyang, B. Gao, Y. Yao, Y. Xue, A. Zimmerman, A. Mosa, P. Pullammanappallil, Y. S. Ok, X. Cao, *Crit. Rev. Environ. Sci. Technol.* **2016**, *46*, 406.
[85] X. Tan, Y. Liu, G. Zeng, X. Wang, X. Hu, Y. Gu, Z. Yang, *Chemosphere* **2015**, *125*, 70.
[86] F. O. Afolabi, P. Musonge, *Molecules* **2023**, *28*, 7050.
[87] X. Xu, X. Cao, L. Zhao, *Chemosphere* **2013**, *92*, 955.
[88] S. Li, F. Yang, Y. Zhang, Y. Lan, K. Cheng, *J. Cleaner Prod.* **2021**, *294*, 125350.
[89] S. Bae, R. N. Collins, T. D. Waite, K. Hanna, *Environ. Sci. Technol.* **2018**, *52*, 12010.
[90] P. Liu, V. M. H. Ng, Z. Yao, J. Zhou, Y. Lei, Z. Yang, H. Lv, L. B. Kong, *ACS Appl. Mater. Interfaces* **2017**, *9*, 16404.
[91] X.-J. Zhang, G.-S. Wang, W.-Q. Cao, Y.-Z. Wei, J.-F. Liang, L. Guo, M.-S. Cao, *ACS Appl. Mater. Interfaces* **2014**, *6*, 7471.
[92] H.-B. Zhao, J.-B. Cheng, J.-Y. Zhu, Y.-Z. Wang, *J. Mater. Chem. C* **2019**, *7*, 441.
[93] B. Wen, M.-S. Cao, Z.-L. Hou, W.-L. Song, L. Zhang, M.-M. Lu, H.-B. Jin, X.-Y. Fang, W.-Z. Wang, J. Yuan, *Carbon* **2013**, *65*, 124.
[94] K. Hu, H. Wang, X. Zhang, H. Huang, T. Qiu, Y. Wang, C. Zhang, L. Pan, J. Yang, *Chem. Eng. J.* **2021**, *408*, 127283.
[95] B. Fan, M. T. Ansar, X. Wang, L. Song, H. Du, H. Lu, B. Zhao, R. Zhang, L. Fan, H. Li, *Adv. Electron. Mater.* **2022**, *8*, 2200169.
[96] B. Liu, W. Song, W. Zhang, X. Zhang, S. Pan, H. Wu, Y. Sun, Y. Xu, *Sep. Purif. Technol.* **2021**, *273*, 118705.
[97] H. Lv, H. Zhang, G. Ji, Z. J. Xu, *ACS Appl. Mater. Interfaces* **2016**, *8*, 6529.
[98] Q. Liu, X. Liu, H. Feng, H. Shui, R. Yu, *Chem. Eng. J.* **2017**, *314*, 320.

[99] Y. Yang, L. Xia, T. Zhang, B. Shi, L. Huang, B. Zhong, X. Zhang, H. Wang, J. Zhang, G. Wen, *Chem. Eng. J.* **2018**, *352*, 510.
[100] H. Lv, Y. Guo, G. Wu, G. Ji, Y. Zhao, Z. J. Xu, *ACS Appl. Mater. Interfaces* **2017**, *9*, 5660.
[101] J. Su, R. Yang, P. Zhang, B. Wang, H. Zhao, W. Zhang, W. Wang, C. Wang, *Diamond Relat. Mater.* **2022**, *129*, 109386.
[102] X. Zhao, D.-M. Guo, Q.-D. An, S.-F. Bo, Z.-Y. Xiao, W.-J. Cai, H.-S. Wang, S.-R. Zhai, Z.-C. Li, *J. Alloys Compd.* **2020**, *822*, 153666.
[103] M. Mahmoodi, B. Aslibeiki, R. Peymanfar, H. Naghshara, *Front. Mater. Sci.* **2022**, *9*, 1088196.
[104] M. Mahmoodi, B. Aslibeiki, M. A. Sakha, M. Zarei, *Mater. Chem. Phys.* **2023**, *300*, 127536.